Multi-Layered Frequency Selective Surfaces for Magnetic Field Shielding in Megahertz Wireless Power Transfer Systems

Wenqiong Chen, Kerui Li, *Member, IEEE*, Bo Xue, Teke Hua, Shu-Yuen Ron Hui, *Fellow, IEEE*, and Alex M. H. Wong, *Senior Member, IEEE*

***Abstract*— As the research paradigm of wireless power transfer (WPT) shifts towards the megahertz (MHz) range, the pronounced hysteresis and eddy current losses within ferromagnetic materials at these frequencies renders existing magnetic shielding techniques neither efficient nor effective. To address this challenging issue, we propose a novel multi-layered frequency selective surface (FSS) magnetic field shielding structure suitable for MHz WPT applications. This design method incorporates multiple FSS layers, each precisely tuned to the fundamental or harmonics of the inverter. By blocking these frequencies, the structure can effectively shield the magnetic fields emitted by wireless power resonators. As an example, a triple-layered FSS (TFSS) is designed and analyzed by conducting full-wave simulation and equivalent circuit model calculation, which operates at the fundamental frequency of 6.78 MHz and two harmonic frequencies. Based on finite element simulation and experimental measurements, the proposed TFSS shield is verified in a 6.78 MHz WPT system. As a result, the TFSS shield strongly suppresses magnetic field leakage (attenuation of about 13.4 dB) with only slight impact on the transfer efficiency of the WPT system (reduction about 1.11% and 2.2% for the WPT system with transmission distances of 1 cm and 10 cm, respectively).**

***Index Terms*—Magnetic field shielding, single-layered frequency selective surface (SFSS), triple-layered frequency selective surfaces (TFSS), power transfer efficiency (PTE), wireless power transfer (WPT).**

I. INTRODUCTION

Wireless power transfer (WPT) technology has attracted considerable attention for its ability to deliver energy efficiently and wirelessly, thereby enhancing the functionality and market value of emerging electronic products [1], [2]. However, its reliance on electromagnetic coupling introduces new challenges, particularly on issues of electromagnetic interference (EMI) and magnetic field shielding. Since WPT systems employ electromagnetic field as the medium for energy exchange, they are inherently susceptible to environmental interference, and may also emit magnetic fields that disturb nearby electronics or raise potential safety concerns, and may degrade overall power transfer efficiency (PTE) [3], [4], [5], [6], [7].

Traditionally, ferromagnetic materials such as ferrite have been widely used as electromagnetic shield in power electronic and WPT systems to confine magnetic flux and suppress stray field leakage. The shielding effectiveness can also be further enhanced by adding a thin conductive layer (such as copper or aluminum) over the ferrite plate [8]. These traditional electromagnetic shields based on conductive and ferromagnetic composites are suitable for a frequency range from tens of kilohertz (kHz) to a few megahertz (MHz) [9], [10], [11], [12], [13], [14], [15], [16], [17]. With the switching speeds of power electronics switches such as gallium nitride (GaN) power switches continue to increase, operating power electronics circuits are expected to increase into the tens of MHz range [18], [19]. In particular, MHz-range WPT systems have been proposed to operate within the Industrial, Scientific and Medical (ISM) frequencies of 6.78 MHz, 13.56 MHz, 27.12 MHz and 40.68 MHz, to comply with global regulations while achieving higher power density, smaller component size, and improved electromagnetic compatibility (EMC) [20], [21], [22]. However, ferromagnetic materials exhibit a sharp decrease in relative permeability and an increase in magnetic loss when operating beyond a few MHz [12]. Alternating magnetic fields induce hysteresis and eddy current power losses in ferromagnetic materials, and such power losses exhibit a positive correlation with the switching frequency. As a result, the PTE and the shielding performance are compromised when conventional ferromagnetic shields are applied in MHz WPT systems [23].

To overcome these limitations, artificial electromagnetic materials and surfaces have been developed for field manipulation and shielding applications in MHz and higher frequency regimes, which are engineered structures with

This work is supported by the Theme Based Research Scheme by the Research Grants Council of Hong Kong, (Grant T23-708/24-N). (*Corresponding author: Alex M. H. Wong*)

Wenqiong Chen and Alex M. H. Wong are with the Department of Electrical Engineering, City University of Hong Kong, Hong Kong, and also with the State Key Laboratory of Terahertz and Millimeter Waves, City University of Hong Kong, Hong Kong (e-mail: wchen336@cityu.edu.hk; alex.mh.wong@cityu.edu.hk).

Kerui Li, Bo Xue and Teke Hua are with the Department of Electrical Engineering, City University of Hong Kong, Hong Kong (e-mail: kerui.li@cityu.edu.hk; boxue3@cityu.edu.hk; tekehua@cityu.edu.hk).

Shu-Yuen Ron Hui is with the Department of Electrical Engineering, City University of Hong Kong, Hong Kong, and also with the Department of Electrical and Electronics Engineering, Imperial College London, SW72X London, U.K. (e-mail: eeronhui@cityu.edu.hk).

Color versions of one or more of the figures in this article are available online at http://ieeexplore.ieee.org

electromagnetic properties unfound in nature [24], [25], [26], [27], [28], [29]. In [24] and [25], two artificial magnetic conductors (AMCs) were designed: one based on a dielectric substrate and the other on a ferrite-dielectric substrate. These designs achieved PTE improvement and magnetic shielding at 26.2 MHz and 6.78 MHz, respectively. In [26], [27], [28], a near-zero permeability metamaterial (MNZ) was applied to reduce magnetic field leakage in 13.56 MHz and 27.12 MHz WPT systems. However, the MNZ encountered a significant efficiency penalty. To complement the design, a negative permittivity metamaterial (MNG) is further incorporated between the transmitter and receiver to improve the PTE of WPT systems. Despite their effectiveness in magnetic field suppression, these shielding structures still face some challenges, including narrow bandwidth, high sensitivity to geometric and electromagnetic parameters, and increased cost and weight, which make it difficult to integrate them into WPT systems.

In recent decades, frequency-selective surfaces (FSSs) have been extensively investigated in microwave and millimeter-wave regimes for EMC and filtering applications [30], [31], [32]. In these studies, multi-layer FSS structures are typically designed to operate in the GHz range, where the unit-cell dimensions are comparable to a significant fraction of the wavelength. Their filtering characteristics mainly rely on plane-wave excitation, spatial phase accumulation, and wave propagation effects. Multi-layer configurations have been widely employed to enhance selectivity, realize dual- or multi-band responses, and improve stopband performance. However, when extending FSS concepts to MHz-band WPT systems, the electromagnetic environment changes fundamentally. At 6.78 MHz, the free-space wavelength is approximately 44m, whereas practical shielding structures are on the order of hundreds of millimeters (or smaller), corresponding to a deep sub-wavelength regime. Under such conditions, the interaction mechanism is dominated by magnetic coupling rather than wave propagation, and the conventional plane-wave-based design methodology is no longer directly applicable.

While progress has been made in applying FSS-based structures to electromagnetic and magnetic shielding in WPT systems, several key limitations remain, particularly in achieving multi-frequency selectivity and balancing shielding performance with transfer efficiency. In [33], a FSS based on a LC resonance design was used as an electromagnetic shield to block GHz EMI from the power inverter circuit in a wireless charging pad in order to enhance signal reception of the mobile phones being charged on the wireless charging pad. Subsequently, a single-layered FSS (SFSS) was recently tested as a magnetic field shield for a wireless power resonator with high quality factor in 13.56 MHz [34], and a cubic wireless charging container featuring an improved Jerusalem FSS coat was reported to effectively prevent electromagnetic radiation leakage from the cubic wireless charging container at 13.56 MHz [35]. However, the SFSS provides shielding only at a particular frequency, whereas in practice, the magnetic field emitted from wireless power resonators contains not only the fundamental frequency but also harmonics generated by the square wave output [36]. Additionally, while the shielding performance of the SFSS is satisfactory at the principal axis, the shielding performance weakens at off-centered locations, and an improvement in magnetic shielding at all locations will advance this technology toward practical deployment.

In this article, we propose a multi-layered FSS design, with each layer tuned to either the fundamental or harmonic components, thereby enabling effective shielding across the entire frequency spectrum. The article is an extended version of a conference paper [37]. The main contributions of this work can be summarized as follows:

(1) A multi-layered FSS architecture is proposed for effective magnetic field shielding in MHz WPT systems, providing stronger suppression and wider bandwidth compared with conventional single-layered design.

(2) A physics-based equivalent circuit model is developed to describe the resonant behavior and coupling mechanism between layers, offering clear physical insight and design guidance.

(3) Comprehensive simulation and experimental validation are conducted on a 6.78 MHz WPT prototype, demonstrating that the proposed FSS achieves significant leakage reduction with minimal impact on power transfer efficiency.

(4) The proposed multi-layered FSS has the advantages of convenient design, low profile and low cost.

II. Models of FSSs and WPT System

A. Single-layered FSS Unit Design

Motivated by the previous works [33], [34] which work at higher frequencies, a compact SFSS is firstly designed to operate at the fundamental frequency of the target 6.78 MHz WPT system. Fig. 1 shows the geometry of the SFSS unit. The SFSS unit is composed of a deformed Jerusalem-cross shaped metallic pattern and four lumped capacitors, as enlarged in Fig.1. The size of the SFSS unit is 496.28 mm × 496.28 mm. The width of the metallic pattern is 32 mm. Here, the four lumped capacitors are 3000pF, respectively. The FSS is printed on a dielectric substrate of FR4 epoxy glass laminate with the relative permittivity of 4.4 and the dielectric loss tangent of 0.02. The thickness of the substrate is 1.6 mm. The key design parameters are labeled in Fig. 1.

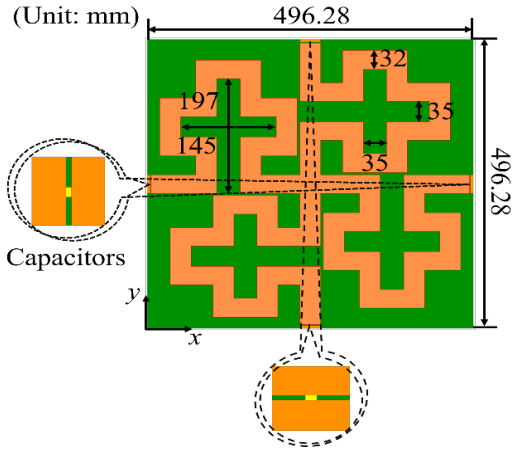

Fig. 1. A schematic diagram of the SFSS.

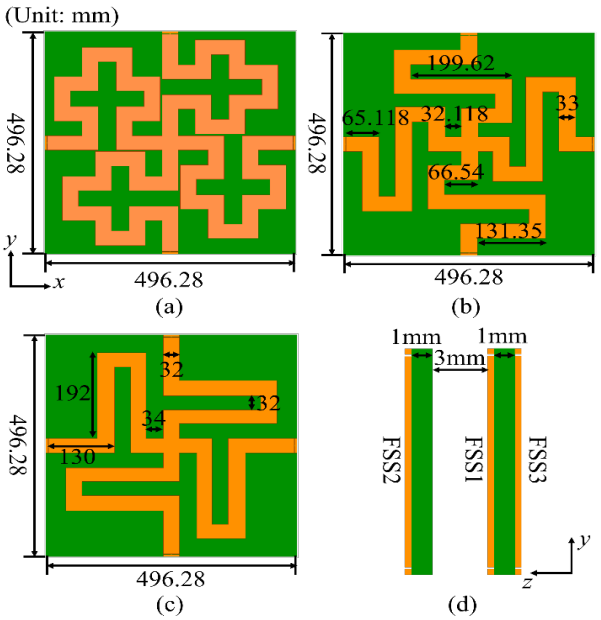

Fig. 2. Schematic of the triple-layered FSS. (a) FSS1, (b) FSS2, (c) FSS3, (d) Side view of TFSS (FSS2 is on the side closer to the Tx coil).

B. Triple-Layered FSS Unit Design

Based on the SFSS, we further propose a multi-layered FSS to operate at both fundamental and harmonic frequencies. Fig. 2 presents the structures of our designed triple-layered FSS (TFSS). Fig. 2(a) to (c) are the front views of the TFSS layers. The first FSS (FSS1) is tuned to operate at the fundamental frequency of 6.78 MHz, which is same with the previously designed SFSS, while the second and the third FSS (FSS2 and FSS3) are separately tuned to operate at the second- and third-order harmonics, at 13.56 MHz and 20.34 MHz. Fig. 2(d) shows the side view of TFSS, where the FSS2 is printed on a single-sided FR4 substrate with the thickness of 1 mm, and positioned as the top layer of the TFSS, while FSS1 and FSS3 are printed on another 1 mm thick double-sided FR4 substrate, and positioned as the second and third layers, respectively. Each FSS is loaded with four lumped capacitors at the ends of the metallic patterns to adjust its resonant frequency. To reduce inter-layer coupling there is a 3 mm air gap between the two substrates. The dimension of each FSS layer is 496.28 mm × 496.28 mm. The widths of the metallic patterns in FSS2 and FSS3 separately are 33 mm and 32 mm. The design parameters of FSS2 and FSS3 are labeled in Fig. 2(b) and (c).

C. Full-Wave Simulation and Equivalent Circuit Analysis of the FSSs

The FSS structures are simulated using the Ansys HFSS finite element method (FEM)-based full-wave electromagnetic software package. Similar to [33, 34], we use the periodic simulation setup, where the FSS is enclosed within periodic boundaries, and a Floquet Bloch wave is used to analyze the scattering properties when a plane wave is incident upon the shield. While the scattered fields in this simulation, which represent the FSS's response to plane wave incidence, themselves are of primary interest in the GHz regime, in our case they serve as a means to obtain component parameters for our equivalent circuit model, which can be applied to analyze both far-field and near-field shielding. As analyzed in [33], the traditional Jerusalem cross-shaped FSS can be equivalent into a LC series circuit, where the inductance is generated by the metallic strip, and the capacitance is arising from the separate gap. Since the FSS structure is symmetric, electromagnetic fields along the vertical and horizontal directions encounter the same equivalent circuit. Fig. 3(a) shows the equivalent circuit model (ECM) of the designed SFSS. The equivalent surface impedance Z_s of the SFSS can be obtained from the equivalent circuit as

$$Z_s = R + j\omega L + \frac{1}{j\omega C} = R + j\left(\omega L - \frac{1}{\omega C}\right) \quad (1)$$

Where C is the capacitance and L is the inductance of the SFSS. When $\omega L = \frac{1}{\omega C}$, $Z_s = R$, so the resonance of the SFSS unit occurs at the frequency f_0:

$$f_0 = \frac{1}{2\pi\sqrt{LC}} \quad (2)$$

In Fig. 3(a), the capacitance value equals to the lumped capacitors and is 3000pF, the inductance value is 184nH, and the resonance frequency of the SFSS is at 6.78 MHz. Fig. 3(b) plots the S parameters for full-wave simulation and equivalent circuit calculation, where S_{11} and S_{21} separately represent the reflection and transmission strengths. It can be concluded that the SFSS exhibits strong reflection (S_{11} is close to 0dB) and low transmission (S_{21} is lower than -10dB) over a wide frequency band. The SFSS acts as a stopband filter at the central filtering frequency of 6.78 MHz.

For our proposed TFSS, each layer can be equivalent into an LC series circuit, so the TFSS can be regarded as a parallel connection of three LC series branches. Fig. 4(a) illustrates the ECM of our TFSS structure, which consists of three coupled resonant sections, each representing one layer of the TFSS. Every section is composed of a capacitor C_i, an inductor L_i and a resistor R_i (i = 1,2,3), forming a parallel RLC resonator that characterizes the capacitance, inductance and loss of each layer, respectively. The inductors L_1, L_2 and L_3 are magnetically coupled with coupling coefficients k_{12}, k_{13} and k_{23}, which represent the electromagnetic interaction among three FSS layers, and the values of inductors depends on the metallic pattern of each layer. The capacitors C_1, C_2 and C_3 are the lumped capacitances loaded at the ends of the metallic patterns, to adjust the three resonant frequencies of TFSS, respectively. The resistors R_1, R_2 and R_3 describe the intrinsic ohmic and dielectric losses within each layer. The self-impedance of each parallel branch can be regarded as

$$Z_{si} = R_i + j\omega L_i + \frac{1}{j\omega C_i} \ (i = 1,2,3) \quad (3)$$

The mutual inductances between different layers can be calculated using the following formula

$$M_{ij} = k_{ij}\sqrt{L_i L_j} \quad (4)$$

For the three-branch parallel circuit, the voltages across the three branches are the same ($V_1 = V_2 = V_3 = V$), and the voltages and currents across the three branches satisfy the

following relation

$$\begin{bmatrix} V_1 \\ V_2 \\ V_3 \end{bmatrix} = \boldsymbol{Z} \begin{bmatrix} I_1 \\ I_2 \\ I_3 \end{bmatrix} \tag{5}$$

Here, the impedance matrix of the TFSS structure ECM can be written as

$$\boldsymbol{Z} = \begin{bmatrix} Z_{s1} & j\omega M_{12} & j\omega M_{13} \\ j\omega M_{12} & Z_{s2} & j\omega M_{23} \\ j\omega M_{13} & j\omega M_{23} & Z_{s3} \end{bmatrix} \tag{6}$$

Then, the equivalent admittance can be obtained by $Y_{eq} = \mathbf{1}^{\mathrm{T}}\boldsymbol{Z}^{-1}\mathbf{1}$. Here, $\mathbf{1}$ is a column vector with all entries equal to 1, of size 3×1. Thus, for the three-branch parallel circuit, the equivalent S parameters can be calculated by

$$\begin{aligned} S_{11} &= \frac{-Y_{eq}Z_0}{2+Y_{eq}Z_0} \\ S_{21} &= \frac{2}{2+Y_{eq}Z_0} \end{aligned} \tag{7}$$

Here, Z_0 is intrinsic impedance of free-space which equals to 377Ω. Table I gives the parameters of the TFSS ECM. The inductances and capacitances are first determined from single-layered FSS simulations, and then finetuned in TFSS simulation to achieve resonant reflection at the desired frequencies. The resistances are tuned to match the resonance depths of S_{21}. The mutual coupling coefficients mainly affect the two resonances of S_{11}. Their values are tuned using the ADS circuit simulation software such that the resultant S_{11} resonances coincide with those observed from the full-wave simulation. Fig. 4(b) presents the comparisons of S_{11} and S_{21} obtained by HFSS simulation and ECM calculation. It can be concluded that there are three resonant frequencies, namely, 6.78 MHz, 13.56 MHz and 20.34 MHz. Further, the close simulation-calculation agreement shows that the equivalent model has indeed captured the dominant electromagnetic properties of the TFSS. Moreover, the S_{11} values at these three frequencies are close to 0dB and the S_{21} values are lower than -20dB at the resonant frequencies, illustrating that the TFSS structure exhibits good electromagnetic wave filtering and low loss performance at the three resonant frequencies.

This coupled resonant configuration enables the circuit to exhibit multiple resonant modes, corresponding to the multi-band frequency selective characteristic observed in full-wave simulations. The mutual coupling terms k_{ij} contribute to the interlayer coupling and energy exchange between each layer, which can either broaden the overall stopband bandwidth or deepen the attenuation. Consequently, the ECM provides a valuable insight into the physical mechanism of the multi-layered FSS, illustrating how resonance coupling among layers enhances the magnetic field suppression performance while maintaining frequency selectivity.

D. Configuration of the WPT system

Fig. 5 shows the configuration of the WPT system. In this article, we use the dual single-layer printed circuit board (PCB) resonators [38] as the transmitter (Tx) and receiver (Rx) to construct the WPT system. Fig. 5(a) is the top view of one PCB board. Here, the circular spiral coil is printed on the PCB board to make a compact resonator. Fig. 5(b) shows the structure of the PCB resonator based on two separate PCB boards with an air gap. The FR4 epoxy glass laminate is used as the PCB board. The dimension of each PCB is 200 mm × 200 mm, the thickness of the PCB substrate is 2 mm, and the linewidth of the copper trace is 8.00 mm. The airgap between two PCB boards is 2 mm. Fig. 5(c) shows the WPT system comprising of two PCB resonators, which is used as Tx and Rx coils, respectively. The WPT system is designed to operate at the 6.78 MHz ISM band. Here, the spacing between two coils is set as D (cm).

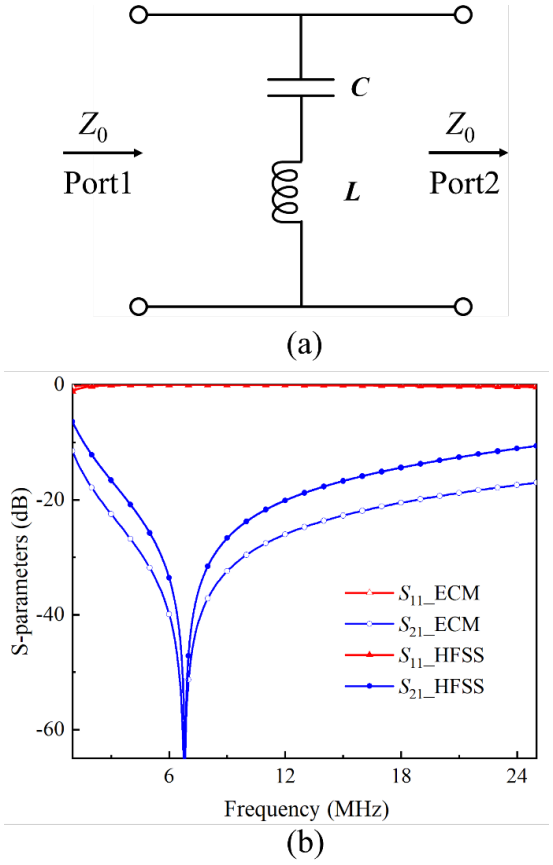

Fig. 3. (a) Equivalent circuit model of the SFSS. (b) Simulated and calculated S_{11} and S_{21} parameters for the SFSS.

TABLE I
PARAMETERS OF THE EQUIVALENT CIRCUIT MODEL OF THE TFSS

Capacitances (pF)	C_1	1200
	C_2	3300
	C_3	820
Inductances (nH)	L_1	125
	L_2	160
	L_3	95
Resistors (Ω)	R_1	0.1
	R_2	0.01
	R_3	1
Mutual coefficients	k_{12}	0.25
	k_{13}	0.25
	k_{23}	0.35

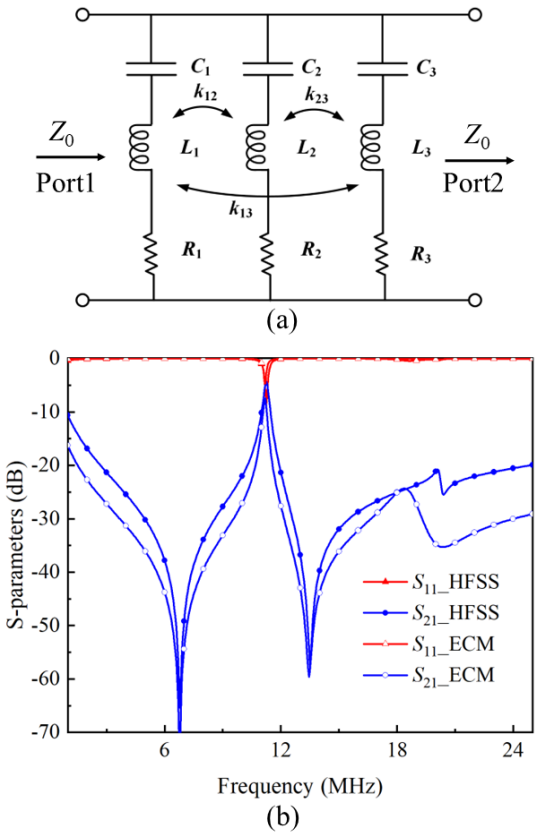

Fig. 4. (a) Equivalent circuit model of the TFSS. (b) Simulated and calculated S_{11} and S_{21} parameters for the TFSS.

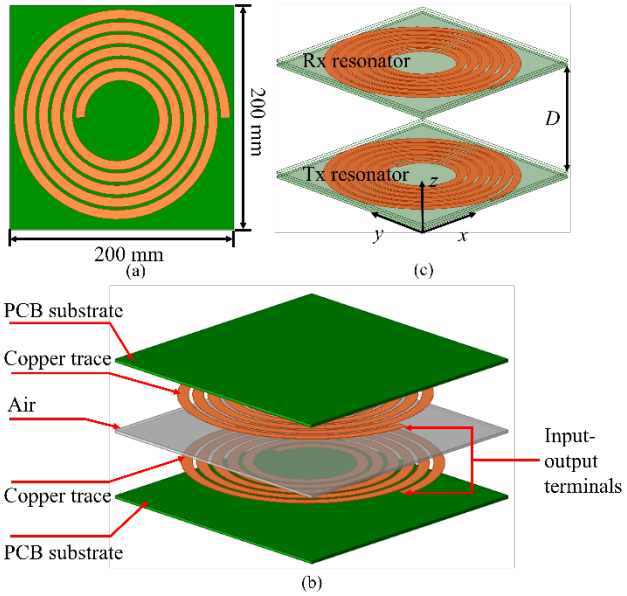

Fig. 5. Schematic of the WPT system. (a) Top view of the PCB board, (b) Structure of the PCB resonator based on two separate PCB boards with an airgap, (c) A WPT system generated by two PCB resonators.

E. Discussion

Fig. 6 summarizes the design flow of the proposed TFSS structure. The three FSS layers are first designed according to the target resonant frequencies f_1, f_2, and f_3 based on the LC resonance principle by tuning the corresponding geometrical and capacitive parameters. An equivalent circuit model is then established to characterize the multi-resonant mechanism of the integrated structure. Finally, the TFSS is incorporated into the WPT system for full-wave simulation, and the design is iteratively optimized by jointly considering magnetic field shielding performance and PTE. This flowchart is added to explicitly clarify the parameter selection and optimization process of the proposed TFSS design.

Specifically, the proposed TFSS consists of three FSS layers, each deliberately designed to operate at a distinct resonant frequency. Unlike a single-layer FSS, which provides a single narrowband stop response centered at its resonance, the TFSS introduces multiple independently engineered resonances. This enables two key design capabilities:

(1) Simultaneous multi-frequency suppression, including both the fundamental operating frequency and higher-order harmonic components.

(2) Higher-order stopband behavior through controlled resonance superposition, rather than mere attenuation enhancement by thickness increase.

Therefore, the contribution is not simply increased shielding magnitude through stacking, but the introduction of a multi-degree-of-freedom resonant design principle, where each layer functions as an independently tunable resonant element. This provides the capability to tailor the magnetic stopband spectrum and extend shielding functionality to harmonic frequencies, which cannot be achieved by a single-layer FSS. In summary, unlike single-layer FSS, which provides only one resonant suppression band, the proposed TFSS supports engineered multi-resonant responses for harmonic suppression. Compared with AMC-based designs, TFSS does not rely on ferrite substrates, vias, or lumped components, thereby avoiding the additional losses and PTE degradation that become more severe at higher WPT frequencies. In contrast to MNZ-based metamaterial shields, TFSS avoids strong dispersion, narrow bandwidth operation, and the need for extra MNG compensation layers, leading to a simpler structure with less impact on system transfer efficiency.

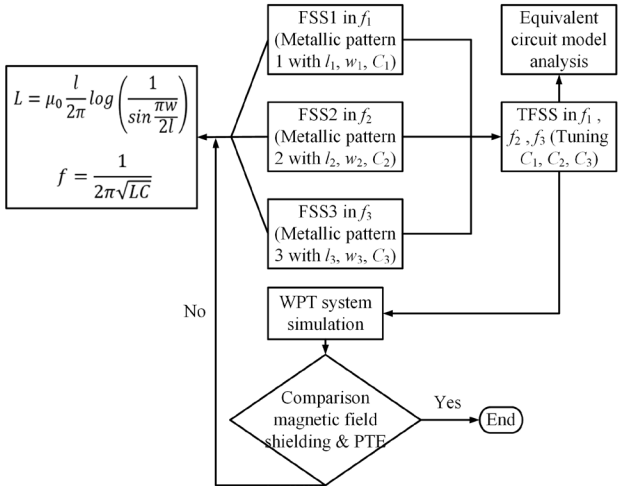

Fig. 6. The design flowchart of the TFSS structure.

III. Simulation Results

A. WPT System with the SFSS Shield

Fig. 7 shows the simulation model of WPT system integrating with SFSS shield, and the distance between Tx and Rx coils is set as D = 10 cm. The SFSS shield is placed on the backside of the Tx coil with a 1 cm spacing. Two observation surfaces are defined to monitor the magnetic field distribution of the WPT system, including the *yoz* plane located at the center section of the model, and the *xoy* plane located 1.5 cm behind the SFSS shield, as shown by the gray planes in Fig. 7(a). The unshielded WPT system is also simulated for benchmarking. Ansys HFSS is used for simulation verification. Separate lumped ports are assigned to the Tx and Rx coils with source powers of 1W and 0W, respectively. An open radiation boundary is applied. The magnetic field distribution and power transfer efficiency (PTE) are recorded during the simulation. In Fig. 8, the normalized magnetic field distributions of two WPT system models are separately drawn on two defined observation planes. As observed in Figs. 8(a) and (b), there are strong magnetic fields behind the Tx coil when there is no shield. As shown in Figs. 8(c) and (d), these magnetic fields can be moderately suppressed using an SFSS shield. However, there still exists some hotspots for SFSS shield at locations away from the principal axis, which were not reported in [33].

B. WPT System with the TFSS Shield

Furthermore, we study the magnetic field distributions of the WPT system with our proposed TFSS shield. Fig. 9 shows the simulation model of the WPT system with TFSS shield, where TFSS shield is placed on the backside of Tx coil with 1 cm spacing. Similarly, two observation planes (shown in gray in Fig. 9) are set to record the magnetic field distributions. Here, the *yoz* plane located at the center section of the model, and the *xoy* plane located 1.5 cm behind the TFSS shield. The simulated magnetic field distributions of the WPT system without and with TFSS are plotted and presented in Fig. 10. It can be seen from Fig. 10(c) and (d), the leakage magnetic field is greatly reduced by the TFSS shield, and the magnetic field strength of hot spots has also been greatly degraded and almost disappeared compared with the SFSS shield results.

To better analyze the magnetic field shieling performance of the two shields, the magnetic field values are extracted along two paths (P1 and P2 as given in Fig. 7(b) and Fig. 9(b)), and plotted in Fig. 10. The relative positions of Rx coil, Tx coil and shield are labeled by dash lines in Fig. 11. In Fig. 11(a), the magnetic field along P1 exhibits a pronounced peak near the transmitter coil with no shields, indicating strong field leakage. While the magnetic field outside the shield region is reduced as SFSS shield is applied, and the TFSS shield further suppresses the magnetic field strength in the region after the shield, demonstrating improved shielding effectiveness. Here, the points with the strongest magnetic fields after SFSS and TFSS shields are labeled, and the same point refer to SFSS shield is labeled for the case of no shield, to quantify the change of magnetic fields without and with shields, as shown in Fig. 11(a). Similarly, Fig. 11(b) presents the magnetic field distribution along P2 path. A comparable trend is observed, where both SFSS and TFSS shields attenuate the magnetic field near the shield region. The turning points of decline are marked for SFSS and TFSS shields, and the value in the same point is shown for no shield case. The conclusion can be obtained that the magnetic field is significantly reduced behind the two shields, however, the TFSS configuration achieves the lowest field magnitude after the shield, confirming its superior capability in mitigating magnetic field leakage while maintain field confinement within the transmitter-receiver region. A detailed quantitative comparison will be given later in the paper.

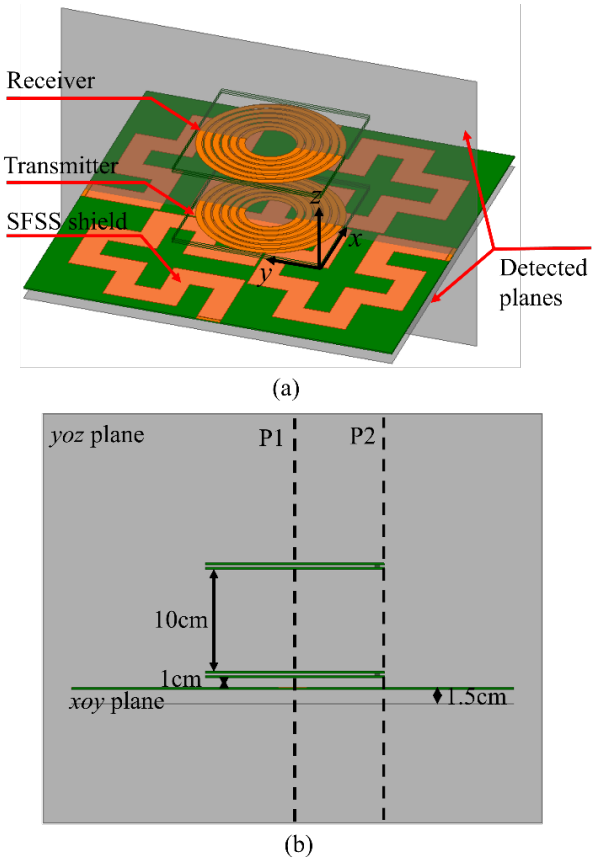

Fig. 7. Simulation model of WPT system with the SFSS shield (D = 10 cm). (a) 3D view, (b) Side view.

C. Misalignment Tolerance

For the misalignment condition, we keep the Tx coil and TFSS shield fixed, only remove the Rx coil laterally causing it to be misaligned with the Tx coil (the misalignment distances change from 0cm to 10cm). As shown in the Fig. 12, the magnetic field along P1 position is obtained under different misalignment distances (Here, the position of P1 is the same as that shown in Fig. 9.). The magnetic field profiles demonstrate that the TFSS consistently suppresses leakage fields across all misalignment conditions. Even at large displacement, the peak magnetic field with TFSS remains significantly lower than the unshielded case, indicating that the multi-resonant suppression mechanism is robust to geometric misalignment. The efficiency comparison shows that while PTE decreases with increasing misalignment for both cases (as expected due to reduced coupling), the efficiency difference between the shielded and unshielded systems remains relatively small (approximately 1.5-2.3% across the entire range). This indicates that the TFSS

does not amplify the sensitivity to misalignment. These results confirm that the proposed TFSS maintains effective magnetic field suppression with only moderate and stable efficiency degradation under practical misalignment conditions, demonstrating robustness and applicability in realistic WPT scenarios.

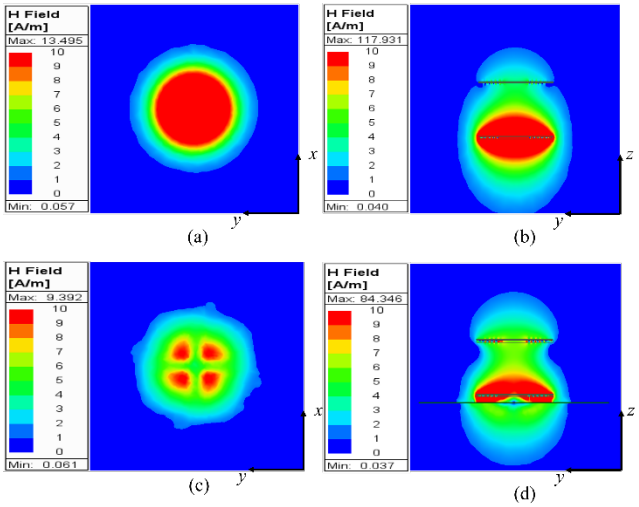

Fig. 8. Simulated magnetic field distribution of the WPT system without and with the SFSS shield on different detected planes. (a)-(b) Without shield on the *xoy* and *yoz* planes. (c)-(d) With the SFSS shield on the *xoy* and *yoz* planes.

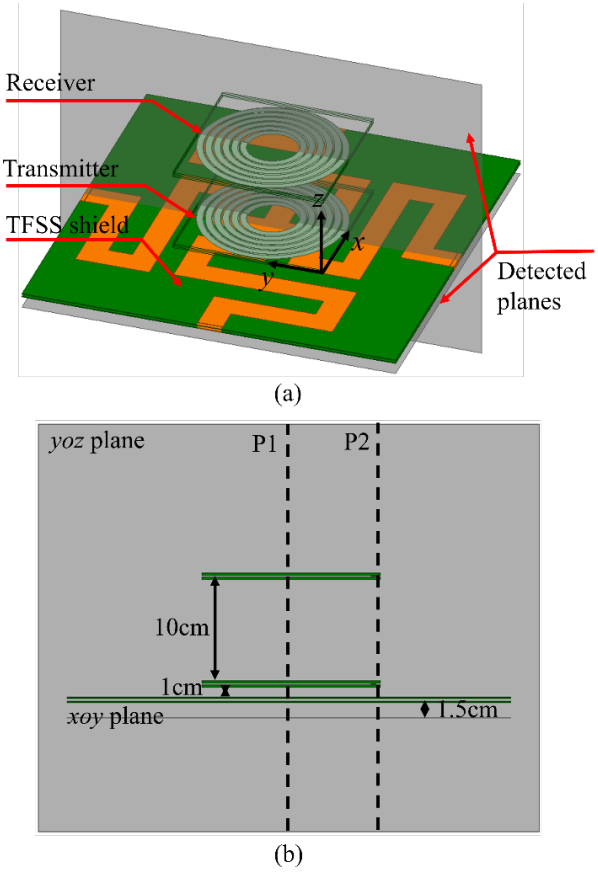

Fig. 9. Simulation model of WPT system with the TFSS shield (D = 10 cm). (a) 3D view, (b) Side view.

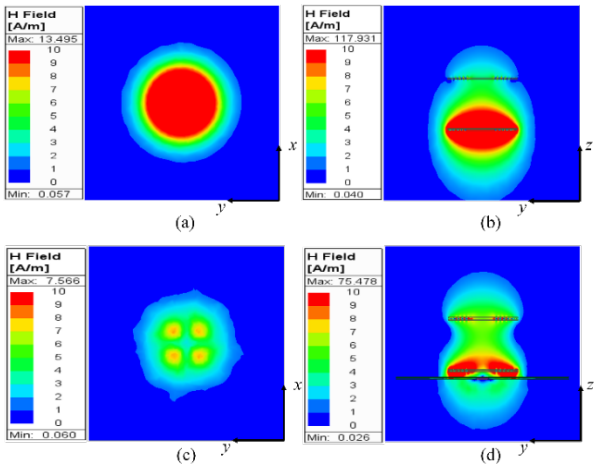

Fig. 10. Simulated magnetic field distribution of the WPT system without and with the TFSS shield on different detected planes. (a)-(b) Without shield on the *xoy* and *yoz* planes. (c)-(d) With the TFSS shield on the *xoy* and *yoz* planes.

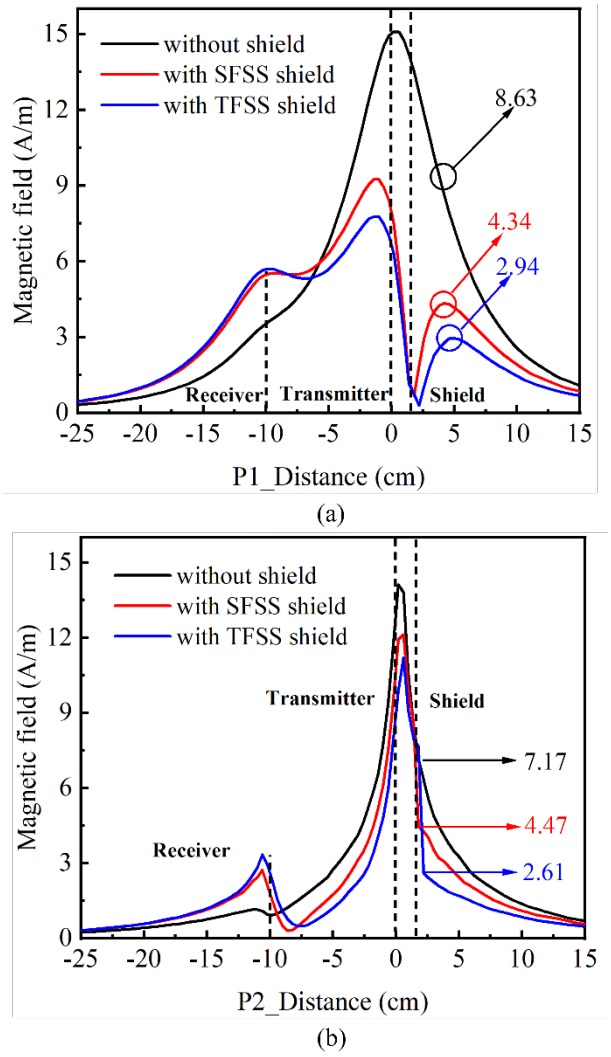

Fig. 11. The extracted magnetic field values of the WPT systems without and with the SFSS and TFSS shields. (a) At the center position (P1). (b) At the edge position (P2). The

locations of the receiver, transmitter, and shield are labelled and shown by dashed lines.

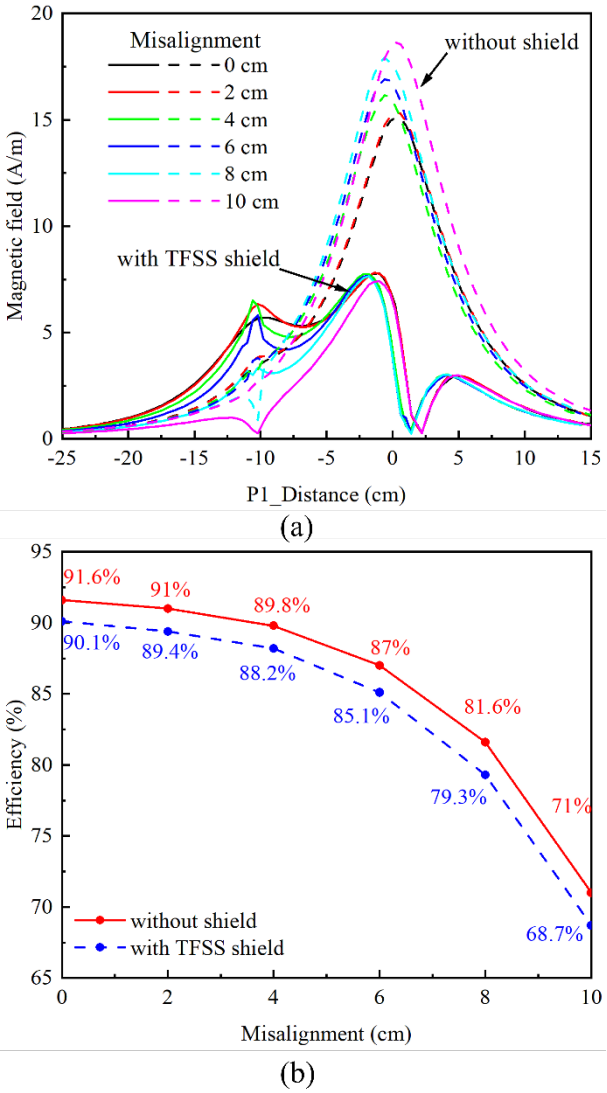

Fig. 12. (a) The extracted magnetic field strengths of the WPT systems under different misalignment conditions without and with the TFSS shield at the center position (P1). (b) Transfer efficiency with the different horizontal misalignment distances.

D. Tolerance to the key design parameters of TFSS shield

To evaluate the robustness of the proposed TFSS shield, a sensitivity analysis was conducted on the key design parameters of the TFSS shield, including the interlayer air gap, metal trace width, capacitor tolerance, and layer sequence. Their influences on the resonant response, shielding attenuation and PTE were systematically investigated. The interlayer air gap has only a minor influence on the electromagnetic response because the structure operates in the quasi-static near-field regime. Simulation results demonstrate that the small spacing variation from 1 mm to 5 mm only causes minor changes in coupling strength, resulting in negligible influence on the shielding performance and PTE. The trace width mainly affects the equivalent inductance and resonant frequency. Excessively narrow traces may reduce shielding effectiveness, while overly wide metallic coverage may increase loss and degrade coupling efficiency. Therefore, the trace width was optimized to achieve a balanced trade-off between shielding attenuation and PTE. The capacitor values directly determine the resonance frequencies. Considering a practical tolerance of ±5%, only slight resonance shifts were observed, while the shielding characteristics and PTE remain stable. In addition, the layer sequence of the three layers affects the coupling distribution and field interaction. An optimized arrangement of the resonant layers ensures well-separated multi-band resonances and stable shielding performance. Although changing the layer order of FSS2 and FSS3 slightly modified the higher-frequency responses, the magnetic shielding capability and PTE remain similar. Overall, the tolerance analysis demonstrates that the proposed TFSS shield possesses strong robustness against design variations and practical fabrication tolerances, while maintaining an effective balance between magnetic shielding performance and high PTE.

IV. Experimental Verification

A. Experimental Setup

Fig. 13 presents the prototypes of the SFSS and the three layers of the TFSS. Fig. 14(a) shows the prototype of the WPT system. Fig. 14(b) shows the experimental setup for testing magnetic field distribution, where a magnetic field probe (i.e., H probe, SinnoRally Type III Large) and a vector network analyzer (VNA, KEYSIGHT E5080A) are used to capture the magnetic field strength along the defined scanning paths. In this experiment, the receiver is terminated by a 50Ω load, and the transmitter and the probe are connected respectively to Port 1 and Port 2 of the VNA. The WPT shields are placed behind the transmitter. The magnetic field distributions are observed on the *xoy* plane (located 1.5 cm away from the shields along the negative *z*-axis), and on the central *yoz* plane (at the plane x = 10 cm, where the coordinate origin is located at the upper right edge of the transmitting coil). The S_{21} parameters of the WPT systems without shield, and with the SFSS shield and with the TFSS shield are separately measured and converted into magnetic field strengths to characterize the magnetic field shielding performance of two shields.

A good shielding structure must significantly reduce the magnetic field leakage and, at the same time, cause minimal effect to the overall transfer efficiency of the WPT system. According to the Ref. [39], the WPT system can be equivalent to a two-port lossy network, where the transmitting port is denoted as Port 1 and the receiving port is denoted as Port 2. The PTE of the WPT system is identical to the transmission efficiency between Port 1 and Port 2, which can be written as

$$\eta = \frac{|S_{21}|^2(1-|\Gamma_L|^2)}{(1-s_{22}\Gamma_L)^2(1-|\Gamma_{in}|^2)} \tag{8}$$

where Γ_{in} is the reflection coefficient at the Port 1, and can be defined as

$$\Gamma_{in} = s_{11} + \frac{s_{12}s_{21}\Gamma_L}{1-s_{22}\Gamma_L}, \tag{9}$$

where Γ_L is the reflection coefficient in relation to the load impedance, which can be calculated as

$$\Gamma_L = \frac{Z_L-Z_0}{Z_L+Z_0}. \tag{10}$$

Here, $Z_0 = 50\Omega$ is the characteristic impedance of the transmission line. The load impedance of the Rx coil we used equals to 50Ω, so the reflection coefficient $\Gamma_L = 0$. The PTE of the WPT system can be calculated by

$$\eta = \frac{|S_{21}|^2}{(1-|S_{11}|^2)} \quad (11)$$

Fig. 14(c) shows the experimental setup for measuring the transfer efficiencies of the WPT systems without shield, and with the SFSS shield and with the TFSS shield, in which the transmitter and receiver are connected respectively to Port 1 and Port 2 of VNA. In this experiment S_{11} and S_{21} can be measured.

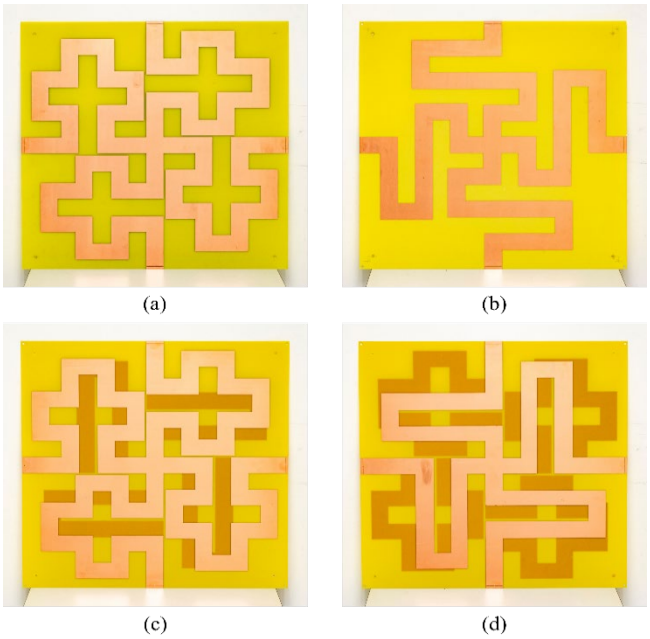

Fig. 13. Photograph of the fabricated FSSs. (a) SFSS, (b-d) The three layers of the TFSS: (b) FSS2, (c) FSS1, and (d) FSS3.

B. Magnetic Field Distributions

Fig. 15 show the measured magnetic field distributions of the WPT systems without shield, with the SFSS shield and with the TFSS shield, respectively, where Fig. 15(a)-(c) are the results on the *xoy* plane, and Fig. 15(d)-(f) are the results on the central *yoz* plane. Here, all measured magnetic fields are normalized into same maximum and minimum values. For the measurement of *yoz* plane, the testing plane is divided into three regions: in front of the Rx coil, between Tx and Rx coils and behind the Tx coil, and measurements are performed separately. As shown in Fig. 15(a), a strong magnetic field can be observed in the central region of *xoy* testing plane, indicating significant magnetic field in the vicinity of the Tx coil for the unshielded WPT system. While introducing the SFSS shield leads to a notable decay in the magnetic field intensity as shown in Fig. 15(b), introducing the TFSS shield further reduces the field amplitude, as presented in Fig. 15(c). This trend can also be observed in the measured results of *yoz* plane, confirming the superior shielding capability of the multi-layered FSS design. In Table II, we extract the maximum magnetic field intensities of the simulation and measurement on the *xoy* detected planes for the WPT systems with no shield, and with SFSS shield and TFSS shield, which are separately normalized to the magnetic strengths without shield. From the simulation results, the magnetic field strength is reduced by 3.29dB with the SFSS shield and 5.11dB with the TFSS shield. In the experiment, it is reduced by 2.93dB with the SFSS shield and 4.65dB with the TFSS shield.

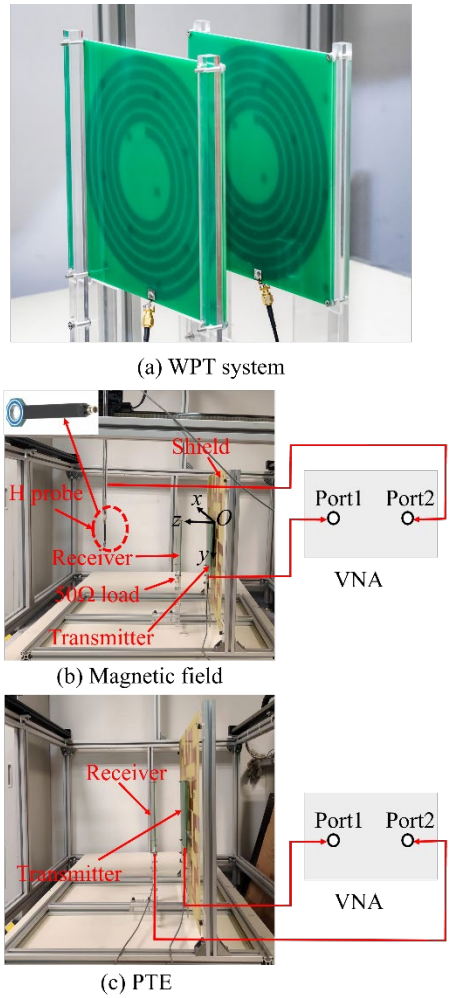

Fig. 14. (a) Prototype of the WPT system. (b) Experimental setup for magnetic field measurement. (c) Experimental setup for PTE measurement.

TABLE II
THE NORMALIZED MAXIMUM MAGNETIC FIELD VALUES OF SIMULATION AND MEASUREMENT FOR THE WPT SYSTEMS WITHOUT AND WITH THE SFSS AND TFSS SHIELDS

Maximum values (dB)	Without shield	With SFSS shield	With TFSS shield
Sim.	0	-3.29	-5.11
Mea.	0	-2.93	-4.65

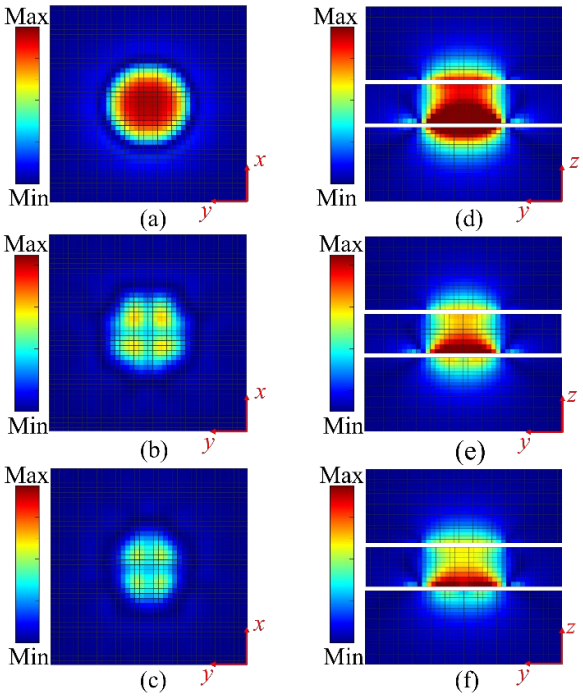

Fig. 15. Normalized measured magnetic field distributions of the WPT system without and with the SFSS and TFSS shields on different detected planes.

C. Power Transfer Efficiencies when D=1cm

We proceed to investigate the effect of the shields on the PTE of the WPT systems. Firstly, we simulate and measure the WPT systems of $D = 1$ cm without and with the SFSS and TFSS shields. Fig. 16 plots the simulated and measured S_{11} (red) and S_{21} (blue) curves, where the dashed curves represent the simulation results and the solid curves denote the experimental measurements. It can be seen that the simulated S parameters are in good agreement with the measurement results in all three cases, especially around the WPT system's operating frequency of 6.78 MHz. The PTE of the WPT system can be calculated through (10) using the S_{11} and S_{21} parameters. Fig. 17(a) gives the simulated PTE results for the three WPT systems as a function of operating efficiency. All three cases exhibit high efficiency operation, exceeding 90% over a broad frequency range. Importantly, the presence of SFSS shield and TFSS shield result in only a negligible reduction in the PTE. Fig. 17(b) plots the corresponding experimental results. The measured efficiency trends consistent with the simulation and the PTE remains higher than 90% from about 6 MHz to 12 MHz. In Table III, the simulated and measured PTE values are listed at the same operating frequency 6.8 MHz. By comparison with the unshielded WPT system, it can be concluded that the PTE has a very little reduction about 0.75% for the WPT system with SFSS shield, and it decreases about 0.98% for the WPT system with TFSS shield in the simulation, and the measured PTE declined by 1.35% with SFSS shield and 1.11% with TFSS shield, showing a negligible efficiency reduction for the WPT system with $D = 1$ cm.

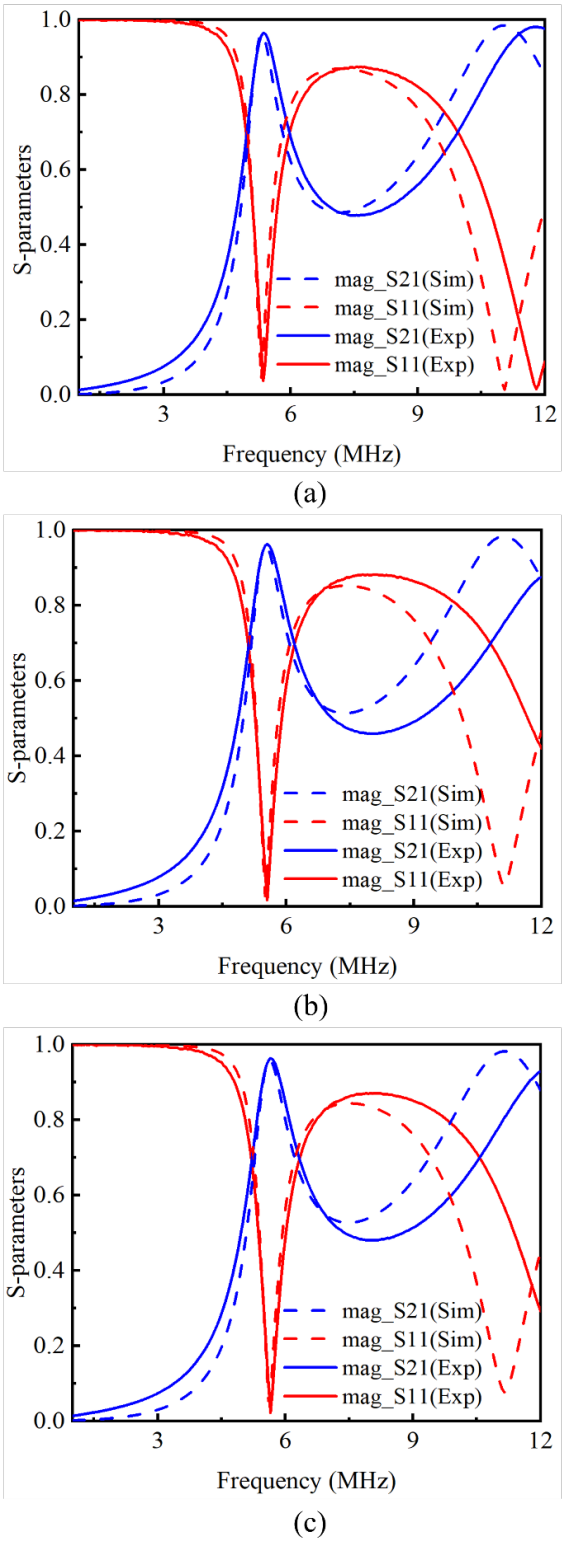

Fig. 16. Simulated and measured S_{11} and S_{21} curves of the WPT systems (D=1 cm) (a) without shield, (b) with the SFSS shield, and (c) with the TFSS shield.

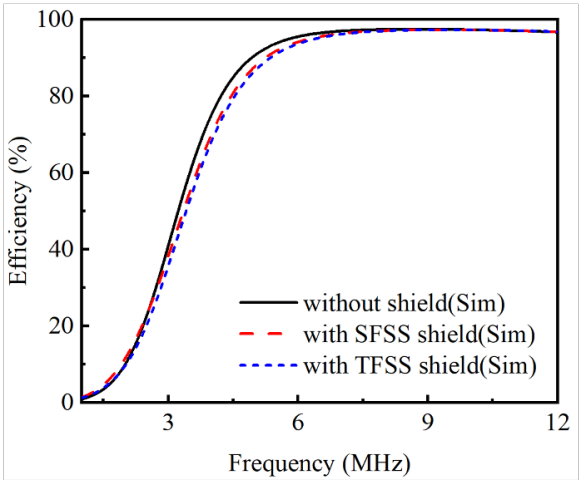

(a)

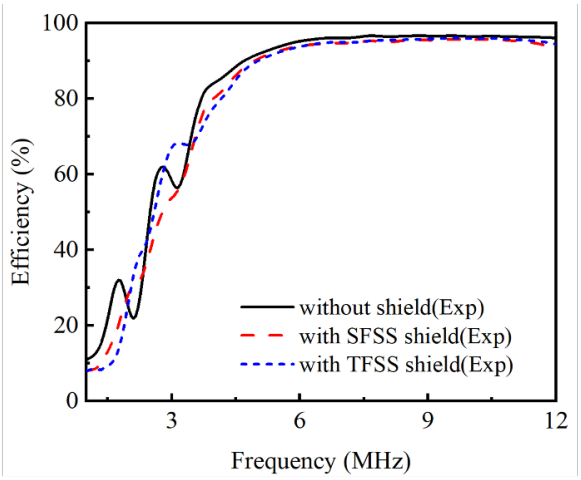

(b)

Fig. 17. (a) Simulated and (b) measured power transfer efficiencies of the WPT systems (D=1 cm) without and with the SFSS and TFSS shields.

TABLE III
COMPARISON OF SIMULATED AND MEASURED MAXIMUM TRANSFER EFFICIENCY OF THE WPT SYSTEMS (D=1CM) WITHOUT AND WITH SFSS AND TFSS SHIELDS AT 6.8 MHZ

	Without shield (Sim/Exp)	With SFSS shield (Sim/Exp)	With TFSS shield (Sim/Exp)
Efficiency (%)	96.85 / 96.07	96.1 / 94.72	95.87 / 94.96

D. Power Transfer Efficiencies when D=10cm

The WPT systems with D = 10 cm and without shield, with the SFSS shield and with the TFSS shield are simulated and measured. In Fig. 18, the magnitude of simulated and measured S_{11} (red) and S_{21} (blue) are plotted as functions of frequency, in which the dashed lines denote the simulation results, and the solid curves represent the measurement results. As shown in the figure, the measured S parameters coincide well with the simulation results, and the S_{21} curves exhibit strong transmission peaks at approximately 6.78 MHz, indicating efficient power transfer at the resonance frequency.

We calculate and plot, in Fig. 19, the PTE of the WPT systems (D = 10 cm) under the three cases: without shield, with the SFSS shield and with the TFSS shield. Fig. 19(a) shows the simulated PTE, where the maximum PTE value is 91.6% and occurs at 6.8 MHz for the WPT system without shield, while the peaks values decrease a little to 90.5% and 90.1%, and the peak frequency shifts to 7.05 MHz and 7.25 MHz when using the SFSS shield and TFSS shield, respectively. In the experiment, as shown in Fig. 19(b), the maximum PTE value is 91.2% at the frequency of 7.05 MHz for the WPT system without shield, while it is 88.8% and the peak frequency shifts to 7.15 MHz for the WPT system with SFSS shield, and the peak PTE decreases to 88.7% and the corresponding frequency shifts to 7.15 MHz for the WPT system with TFSS shield. In Table IV, the simulated and measured maximum PTE values and the peak frequencies of the WPT systems without and with SFSS and TFSS shields are listed in detail. By comparison, it can be obtained that the maximum PTE only decreases by around 1.1% with the SFSS shield and 1.5% with the TFSS shield in the simulation, and the experimental PTE decreases by around 2.4% with the SFSS shield and 2.5% with the TFSS shield, compared to the unshielded WPT system. Here, minor deviations of resonance frequency and PTE curves in simulation and measurement can be attributed to the fabrication tolerances and measurement setup imperfections. Subsequent finetuning should be able to shift the PTE peak back to the desired WPT frequency of 6.78 MHz. Our results verify that the proposed TFSS shield provides effective shielding performance with minimal degradation in power transfer efficiency.

E. Power Transfer Efficiencies with Different Coil Separation Distances

We proceed to study the transfer efficiency change of the WPT systems with different distances D under two cases: without shield and with TFSS shield. In Fig. 20, we plot the simulated and measured PTE of the two WPT systems versus the separation distance D between two coils. It can be observed that the PTE decreases with increasing D due to the reduced magnetic coupling between two coils, and the TFSS shield exhibits negligible impact on transfer efficiency across the entire distance range. Small differences between simulation and measurement may have arisen from the fabrication tolerances of coils and shield, additional parasitic losses (such as cables, connectors) and minor misalignment during distance sweeps. Overall, these results confirm that the proposed TFSS effectively preserves the PTE over distance while enabling magnetic-field shielding, satisfying the key requirements for low-loss integration into practical WPT systems.

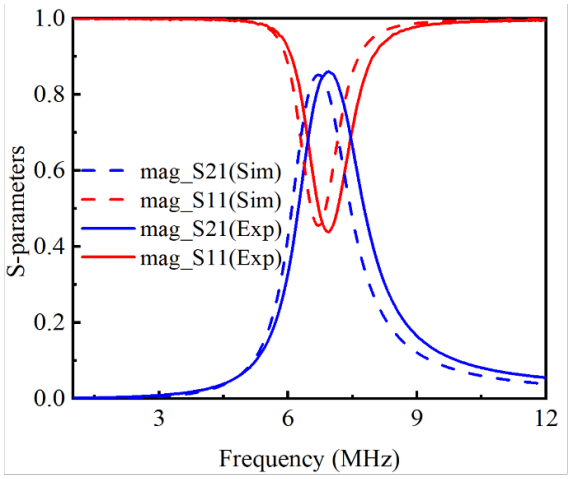

(a)

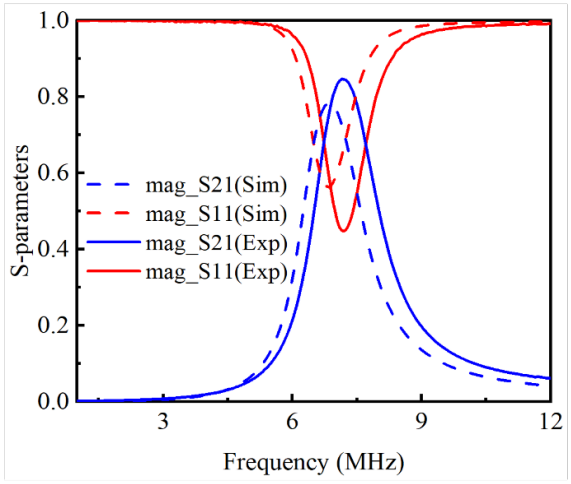

(b)

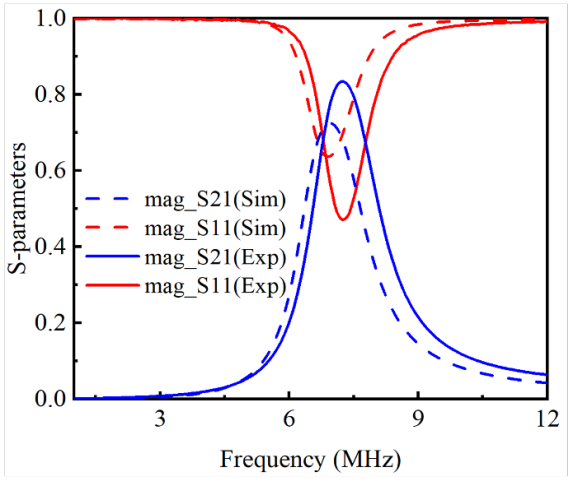

(c)

Fig. 18. Simulated and measured S_{11} and S_{21} curves of the WPT systems (D=10 cm) (a) without shield, (b) with the SFSS shield, and (c) with the TFSS shield.

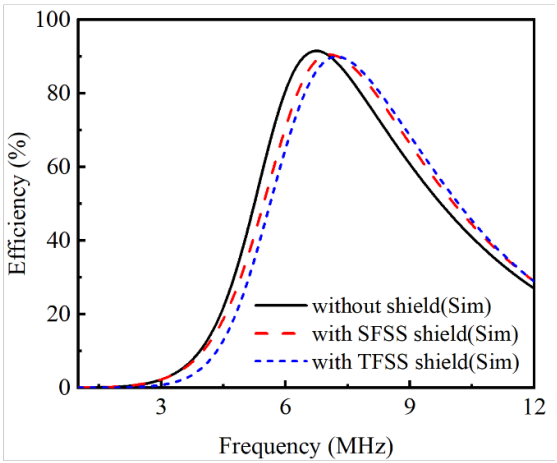

(a)

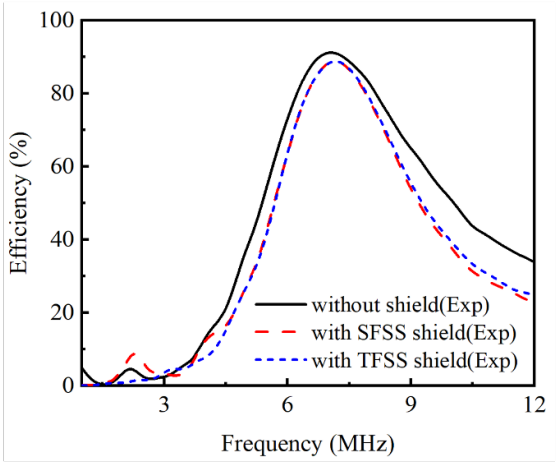

(b)

Fig. 19. (a) Simulated and (b) measured power transfer efficiencies of the WPT systems (D=10 cm) without and with the SFSS and TFSS shields.

TABLE IV
COMPARISON OF SIMULATED AND MEASURED MAXIMUM TRANSFER EFFICIENCY OF THE WPT SYSTEMS (D=10CM) WITHOUT AND WITH SFSS AND TFSS SHIELDS

	Without shield (Sim/Exp)	With SFSS shield (Sim/Exp)	With TFSS shield (Sim/Exp)
Efficiency (%)	91.6 / 91.2	90.5 / 88.8	90.1 / 88.7
Frequency (MHz)	6.8 / 7.05	7.05 / 7.15	7.25 / 7.15

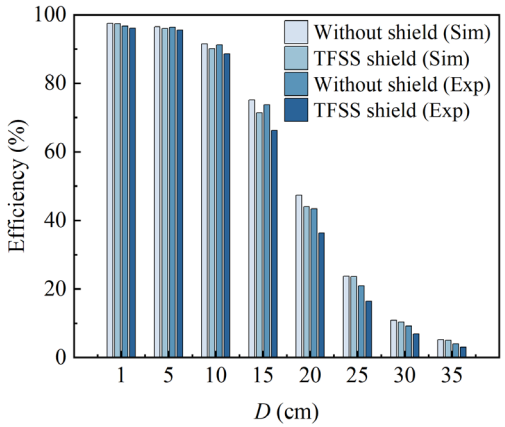

Fig. 20. Simulated and measured power transfer efficiencies of the WPT systems under different *D* (cm) without and with the TFSS shield.

F. Shielding Performance and PTE Measurements with a DC-AC Inverter

To verify the shielding performance of the TFSS shield against higher harmonic components, we test the experimental prototype in a high-power test apparatus as shown in Fig. 21. The ITEC DC power supply is used. The self-resonant transmitter is fed by a high-frequency AC input voltage that is generated by a GaN switch (GSB61008T) based half-bridge inverter. The half-bridge inverter is operated with a duty cycle of 0.47. The dead time is set to 17ns. The PWM signals are generated by a signal generator (AFG31000 SERIES). The load resistor is 50Ω. The inverter spectrum, as shown in Fig. 22, is predominantly composed of the fundamental and third harmonic components. Since higher harmonic components have less than 2% the power of the fundamental component, our choice to exclude FSS-layers targeting these harmonics does not appreciably degrade the shielding performance.

Here, we select two test points behind the WPT systems with about 1.5 cm, i.e. center position and off-center position (far away from the center position with about 5 cm). The magnetic field is captured by a H-probe and observed on MXO44 oscilloscope. The measured results of the WPT systems without shield and with SFSS and TFSS shields are shown in Fig. 23, respectively. The input DC power supply is set as 50V and the input power is about 45W. As can be seen in Fig. 23(a)-(c), the magnetic field at the central location is 5.2dBm at the fundamental frequency (6.8 MHz) and -19.6dBm at the third harmonic frequency (20.4 MHz) for the WPT system without shield. When using the SFSS shield, it is only reduced by 8.2dBm at the fundamental frequency, and the third harmonics keeps almost unchanged. However, when using the TFSS shield, both the fundamental and harmonic components are separately reduced by 13.4dB and 12.2dB. From Fig. 23(d)-(f), the magnetic field at the off-centered location is about -1dBm in the fundamental frequency and -22.2dBm in the third harmonic frequency for the WPT system without shield. Only the fundamental component is reduced to -5.4dBm by the SFSS shild and the third harmonic component is unattenuated. On the other hand, the magnetic field at the fundamental frequency is reduced by 10.8dB and the magnetic field at the third harmonics is reduced by 13.4dB for the TFSS shield. Thus the proposed TFSS shield exhibits better shielding effect not only at the fundamental frequency but also at the higher harmonics.

To further validate the multi-frequency shielding capability of the TFSS structure, three sinusoidal signals at the fundamental, second, and third harmonic frequencies are directly injected, keeping the same amplitude under the unshielded and with TFSS shield cases. This approach provides a more controlled and independent evaluation of shielding performance at each frequency component. The magnetic field of the WPT systems is tested at the center point, as shown in Fig. 24. The results show that all three frequency components are clearly observable without the shield, while the magnetic field amplitudes at all three frequencies are significantly reduced with the TFSS shield. The shielding effect remains effective across the fundamental, second, and third harmonics, confirming the multi-frequency suppression capability of the proposed TFSS.

When the DC input voltage is 50V and the operating frequency is tuned to the self-resonant frequency of the WPT systems without and with SFSS and TFSS shields, the measured voltage and current waveforms from MXO44 are shown in Fig. 25. It should be noted that the gating window of the oscilloscope is adjusted to encompass an integer number of cycles corresponding to the operating frequency to ensure accurate power measurement, allowing us to average the instantaneous power over complete periods and minimize errors due to partial cycles or transients. Fig. 26 gives the received power distributions under different DC input voltages. It can be obtained that the test power can reach 40W, and the transfer efficiency is about 88.5% for the WPT system without shield, the transfer efficiency is 87.4% for the WPT system with the SFSS shield, the transfer efficiency is 86.3% for WPT system with TFSS shield. The PTE decreases by only 2.2% for the TFSS shield. These results show the ability of the TFSS shield to perform magnetic field shielding and maintain the PTE up to a moderately input high power level of 45W.

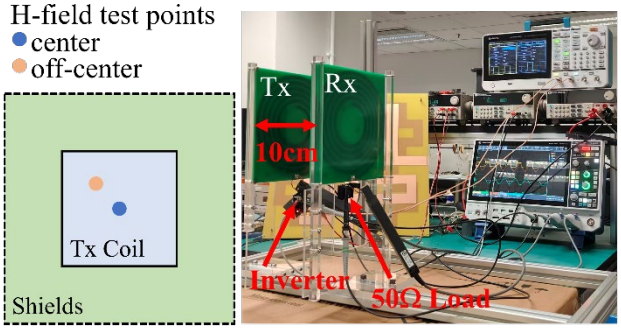

Fig. 21. Prototype to measure the magnetic field at different points behind the WPT systems with about 1.5cm.

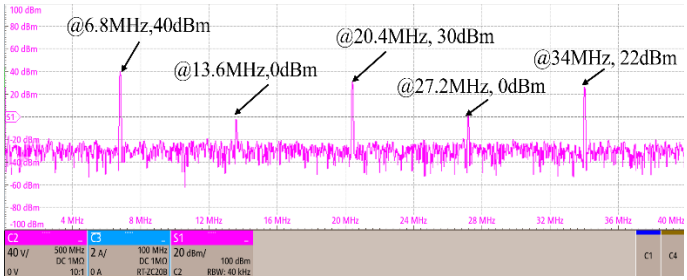

Fig. 22. The measured spectrum result of the actual inverter.

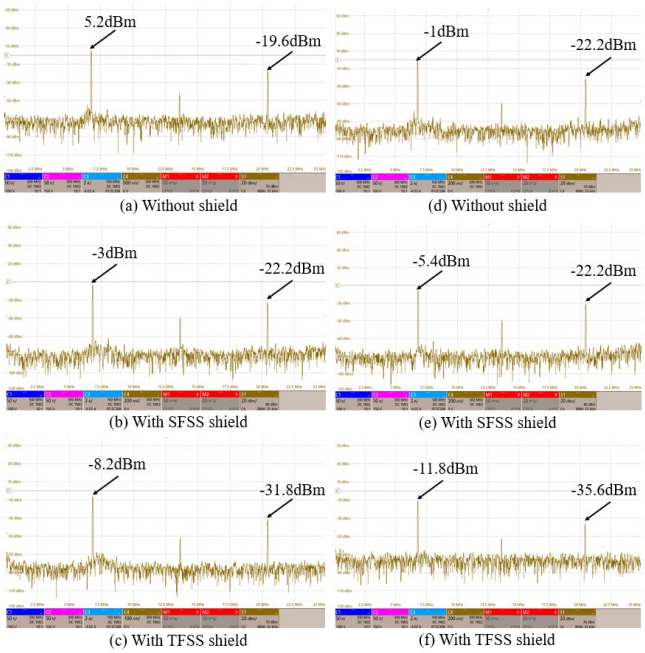

Fig. 23. Magnetic field tests of the WPT systems without and with the SFSS and TFSS shields at different points. (a)-(c) Magnetic field at center point. (d)-(f) Magnetic field at off-center point.

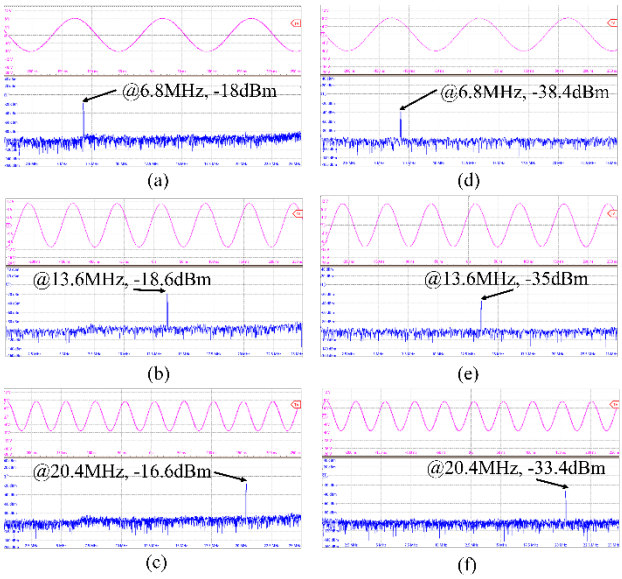

Fig. 24. Magnetic field tests of the WPT systems under the injection of three sinusoidal signals at the fundamental, second, and third harmonic frequencies. (a)-(c) Without shield at the center point. (d)-(f) With the TFSS shield at the center point.

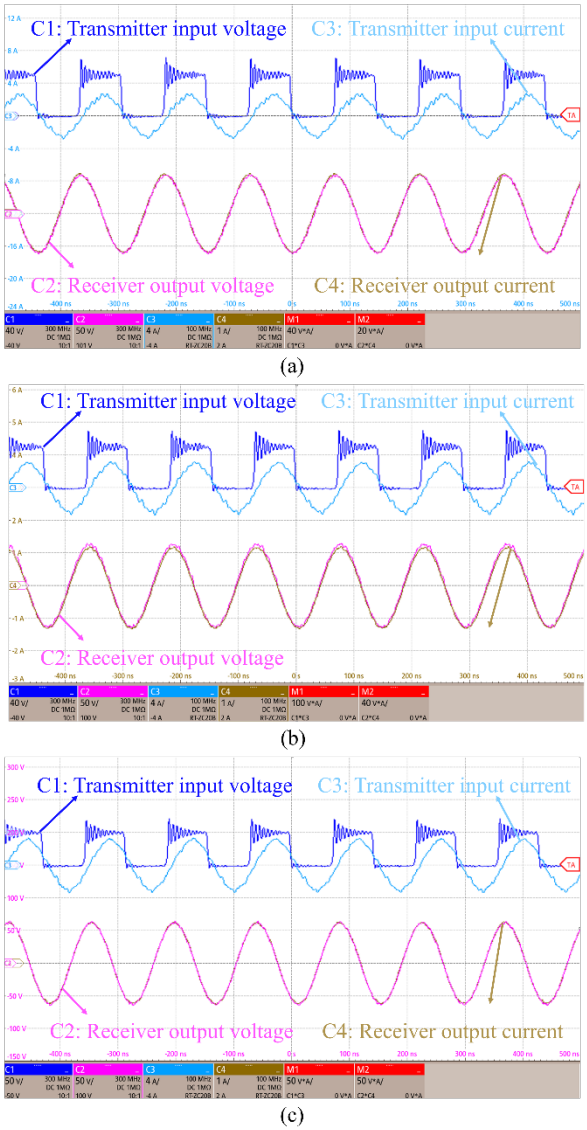

Fig. 25. Measured voltage waveforms, current waveforms of the WPT systems under 50V DC power supply. (a) Without shield. (b) With the SFSS shield. (c) With the TFSS shield.

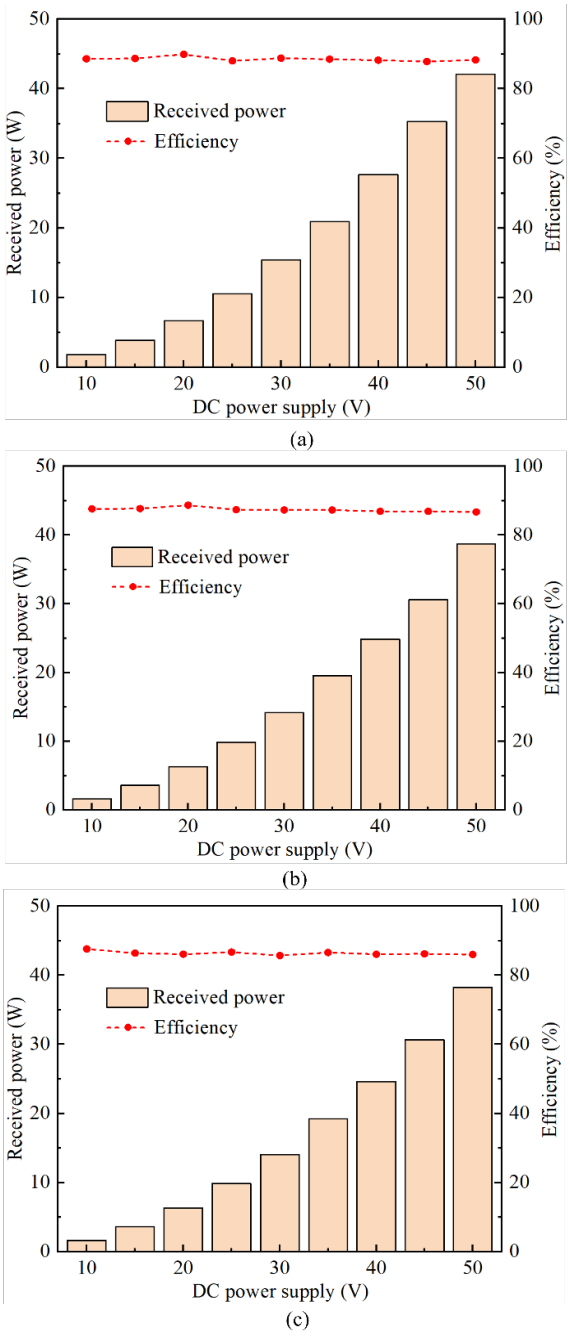

Fig. 26. Received power and efficiency distributions under different DC input voltages. (a) Without shield. (b) With the SFSS shield. (c) With the TFSS shield.

V. Conclusion

In this article, a multi-layered FSS design for magnetic field shielding in the MHz WPT system operating is presented. A novel TFSS shield design is developed based on an earlier SFSS shield design. While the SFSS shield only can operate at the single resonant frequency, the TFSS shield can operate at the fundamental resonant frequency and two higher harmonics. The resonant characteristics of the TFSS unit is analyzed by full wave simulation, and the corresponding ECM is built to characterize the dominant operation mechanism of the multi-layered FSS. The WPT systems with three cases (i.e., without shield, with SFSS shield, with TFSS shield) are simulated by finite element method and experimentally measured. Compared with the single-layered design, this triple-layered design more effectively blocks the magnetic field emissions at the fundamental frequency, the second-order and third-order harmonics, but also achieves superior leakage magnetic field attenuation. Essentially, the transfer efficiency is minimally affected. It should also be noted that the proposed TFSS is intended for medium-power MHz WPT systems, where its physical size is mainly determined by the magnetic flux coverage requirement of the resonator, meanwhile, the underlying multi-resonant design concept remains scalable to future miniaturized or foldable implementations. These research results demonstrate that the proposed multi-layered FSS design provides a promising solution to the long-standing electromagnetic shielding issue in multi-Mega-Hertz WPT systems. Overall, Table V is given to clarify the difference and advantages of our proposed TFSS shield, compared with other existing shielding techniques. The proposed TFSS shield employs low-cost FR4 substrates and simple PCB fabrication, avoiding the use of expensive and difficult-to-process ferrite materials, while simultaneously suppressing the fundamental and harmonic components with excellent shielding performance and only minimal efficiency degradation.

TABLE V
COMPARISON OF TFSS SHIELD WITH OTHER SHIELDS

	Ferrite		AMC		MNZ		SFSS	This work
Ref.	[17]	[16]	[24]	[25]	[28]	[27]	[33]	
Shield Size	$2.2L_c \times 1.3W_c$	$\approx 1.13L_c \times 1.13W_c$	$4.64L_c \times 4.64W_c$	$3.52L_c \times 3.52W_c$	$1.6L_c \times 1.6W_c$	MNZ:$1.4L_c \times 1.4W_c$ MNG:$4.2L_c \times 4.2W_c$	$\approx 1.1L_c \times 2W_c$	$2.484L_c \times 2.484W_c$
Thickness	45 mm	0.2 mm	5 mm	6.6 mm	2 mm	MNZ: ≈4.8mm MNG:13.2mm	0.5 mm	5 mm
Resonant Frequency	30 kHz	6.78 MHz	26.2 MHz	6.98 MHz	13.56 MHz	13.56, 27.12 MHz	850-1200 MHz	6.78, 13.56, 20.34 MHz
Design Category	Ferrite + Aluminum plate	Ferrite + copper plate	Dielectric substrate + metallic patterns / vias + capacitors	Ferrite + dielectric substrate + metallic patterns / vias + capacitors	Only MNZ	DB-MNZ + DB-MNG	Single FSS	Three FSS layers
Processing technology (cost and weight)	Ferrite plate (high, heavy)	Ferrite plate (high, heavy)	PCB and metallic vias (medium, medium)	PCB, vias, custom perforated ferrite board (high, weight)	PCB (low, light)	PCB (low, weight)	PCB (low, light)	PCB (low, light)
Shielding Effect (%)	≈91%	98%	NA*	88%	≈85%	36%, 59%	NA*	79%, 76%
ΔPTE (%)	+7.3% at 20cm	-3.5%	+19% at 3cm	+8% at 10cm	-24.2% at 30cm	+28.86%, +10.49% at 20cm	-0.49%	-2.2% at 10cm
Measurement condition	High power (large signal)	Network Analyzer (small signal)	Network Analyzer (small signal)	Network Analyzer (small signal)	Network Analyzer (small signal)	Network Analyzer (small signal)	Network Analyzer (small signal)	Network Analyzer (small signal) + High power (large signal)

L_c & W_c are the length and width of the coil, the shield size is normalized relative to the coil dimension.
NA* is not available.
The shielding effect (SE) is normalized as $SE = (1 - X_{shield}/X_{no}) \times 100\%$. dB/dBm values are converted to linear ratios before normalization.

REFERENCES

[1] A. Alabsi *et al.*, "Wireless Power Transfer Technologies, Applications, and Future Trends: A Review," *IEEE Trans. Sustain. Comput.*, vol. 10, no. 1, pp. 1–17, Jan. 2025.
[2] A. Laha, A. Kalathy, M. Pahlevani, and P. Jain, "A Comprehensive Review on Wireless Power Transfer Systems for Charging Portable Electronics," *Eng*, vol. 4, no. 2, pp. 1023–1057, Apr. 2023.
[3] S. Hong *et al.*, "A Frequency-Selective EMI Reduction Method for Tightly Coupled Wireless Power Transfer Systems Using Resonant Frequency Control of a Shielding Coil in Smartphone Application," *IEEE Trans. Electromagn. Compat.*, vol. 61, no. 6, pp. 2031–2039, Dec. 2019.
[4] C. Lee, S. Woo, Y. Shin, J. Rhee, J. Moon, and S. Ahn, "EMI Reduction Method for Wireless Power Transfer Systems with High Power Transfer Efficiency Using Frequency Split Phenomena," *IEEE Trans. Electromagn. Compat.*, vol. 64, no. 5, pp. 1683–1693, Oct. 2022.
[5] S. A. Chowdhury, S.-W. Kim, S.-M. Kim, J. Moon, I.-K. Cho, and D. Ahn, "Automatic Tuning Receiver for Improved Efficiency and EMI Suppression in Spread-Spectrum Wireless Power Transfer," *IEEE Trans. Ind. Electron.*, vol. 70, no. 1, pp. 352–363, Jan. 2023.
[6] C. Wu, H. Kim, S. Penugonda, and J. Fan, "Analysis and Modeling of the Common-Mode Conducted EMI From a Wireless Power Transfer System for

Mobile Applications," *IEEE Trans. Electromagn. Compat.*, vol. 63, no. 6, pp. 2143–2150, Dec. 2021.
[7] C. Song *et al.*, "EMI Reduction Methods in Wireless Power Transfer System for Drone Electrical Charger Using Tightly Coupled Three-Phase Resonant Magnetic Field," *IEEE Trans. Ind. Electron.*, vol. 65, no. 9, pp. 6839–6849, Sep. 2018.
[8] S. C. Tang, S. Y. Hui, and H. S.-H. Chung, "Evaluation of the shielding effects on printed-circuit-board transformers using ferrite plates and copper sheets," *IEEE Trans. Power Electron.*, vol. 17, no. 6, pp. 1080–1088, Nov. 2002.
[9] A. Yadav and T. K. Bera, "Ferrite shielding thickness and its effect on electromagnetic parameters in wireless power transfer for electric vehicles (EVs)," *J. Eng. Appl. Sci.*, vol. 70, no. 1, p. 132, Dec. 2023.
[10] R. Qin, J. Li, J. Sun, and D. Costinett, "Shielding Design for High-Frequency Wireless Power Transfer System for EV Charging with Self-Resonant Coils," *IEEE Trans. Power Electron.*, vol. 38, no. 6, pp. 7900–7909, Jun. 2023.
[11] C. A. Stergiou and V. Zaspalis, "Impact of Ferrite Shield Properties on the Low-Power Inductive Power Transfer," *IEEE Trans. Magn.*, vol. 52, no. 8, pp. 1–9, Aug. 2016.
[12] W. Lee *et al.*, "A Simple Wireless Power Charging Antenna System: Evaluation of Ferrite Sheet," *IEEE Trans. Magn.*, vol. 53, no. 7, pp. 1–5, Jul. 2017.
[13] D. B. Ahire, V. J. Gond, and J. J. Chopade, "Coil material and magnetic shielding methods for efficient wireless power transfer system for biomedical implant application," *Biosensors and Bioelectronics: X*, vol. 10, p. 100123, May 2022.
[14] C. Rong, X. Tao, C. Lu, and M. Liu, "Investigation of Magnetic Field Shielding by Mesh Aluminum Sheet in Wireless Power Transfer System," in *2019 IEEE Wireless Power Transfer Conference (WPTC)*, London, UK: IEEE, Jun. 2019.
[15] V. Chakibanda and V. L. N. Komanapalli, "Investigation on Optimizing Aluminum Shield for Improved Performance in Inductively Coupled Wireless Power Transfer System," *IEEE Access*, vol. 13, pp. 180413–180433, 2025.
[16] N. S. Tran Bui, C. D. Pham, T. T. Ha Le, and M. T. Le, "A 6.78-MHz Free-Positioning Wireless Charging Bowl with Optimized Passive Electromagnetic Shield for Wearable Devices," in *2024 5th International Conference on Smart Sensors and Application (ICSSA)*, Penang, Malaysia: IEEE, Sep. 2024, pp. 1–5.
[17] H. Kim, J. Cho, S. Ahn, J. Kim, and J. Kim, "Suppression of leakage magnetic field from a wireless power transfer system using ferrimagnetic material and metallic shielding," in *2012 IEEE International Symposium on Electromagnetic Compatibility*, Pittsburgh, PA, USA: IEEE, Aug. 2012, pp. 640–645.
[18] L. Díaz, M. Sivolella, P. Pérez-Nicoli, and F. Silveira, "Wirelessly Programmable Class-E GaN-Based 13.56 MHz Transmitter for Wireless Power Transfer," in *2024 IEEE 15th Latin America Symposium on Circuits and Systems (LASCAS)*, Punta del Este, Uruguay: IEEE, Feb. 2024, pp. 1–5.
[19] L. Jiang and D. Costinett, "A High-Efficiency GaN-Based Single-Stage 6.78 MHz Transmitter for Wireless Power Transfer Applications," *IEEE Trans. Power Electron.*, vol. 34, no. 8, pp. 7677–7692, Aug. 2019.
[20] Z. Ye, M. Yang, and P.-Y. Chen, "Multi-Band Parity-Time-Symmetric Wireless Power Transfer Systems for ISM-Band Bio-Implantable Applications," *IEEE J. Electromagn. RF Microw. Med. Biol.*, vol. 6, no. 2, pp. 196–203, Jun. 2022.
[21] A. Bharadwaj and M. J. Makhetha, "Integrated Resonant Track for High-Efficiency Wireless Power Transfer in ISM Bands," in *2025 IEEE Wireless Power Technology Conference and Expo (WPTCE)*, Rome, Italy: IEEE, Jun. 2025, pp. 1–5.
[22] A. Clements, V. Vishnoi, S. Dehghani, and T. Johnson, "A Comparison of GaN Class E Inverter and Synchronous Rectifier Designs for 13.56 MHz, 27.12 MHz and 40.68 MHz ISM Bands," in *2018 IEEE Wireless Power Transfer Conference (WPTC)*, Montreal, QC, Canada: IEEE, Jun. 2018, pp. 1–4.
[23] S. Y. R. Hui, C. Zhang, K. Li, A. M. H. Wong, and S. C. Tan, "Some Key Aspects of Near-Field Wireless Power Transfer Technologies for High Frequency, High Power and High Efficiency," *IEEE Trans. Power Electron.*, pp. 1–18, 2025.
[24] T. Shi *et al.*, "Using artificial magnetic conductors to improve the efficiency of wireless power transfer," *AIP Advances*, vol. 9, no. 4, p. 045308, Apr. 2019.
[25] S. M. Radha, S. H. Choi, J. H. Lee, J. H. Oh, I.-K. Cho, and I.-J. Yoon, "Ferrite-Loaded Inverted Microstrip Line-Based Artificial Magnetic Conductor for the Magnetic Shielding Applications of a Wireless Power Transfer System," *Applied Sciences*, vol. 13, no. 18, p. 10523, Sep. 2023.
[26] C. Lu *et al.*, "Investigation of Negative and Near-Zero Permeability Metamaterials for Increased Efficiency and Reduced Electromagnetic Field Leakage in a Wireless Power Transfer System," *IEEE Trans. Electromagn. Compat.*, vol. 61, no. 5, pp. 1438–1446, Oct. 2019.
[27] C. Lu, X. Huang, C. Rong, X. Tao, Y. Zeng, and M. Liu, "A Dual-Band Negative Permeability and Near-Zero Permeability Metamaterials for Wireless Power Transfer System," *IEEE Trans. Ind. Electron.*, vol. 68, no. 8, pp. 7072–7082, Aug. 2021.
[28] C. Rong *et al.*, "A Comprehensive Analysis of Metamaterial-Coupled WPT Systems for Low Electromagnetic Field Leakage," *IEEE Trans. Electromagn. Compat.*, vol. 65, no. 1, pp. 166–176, Feb. 2023.
[29] M. M. Masud, B. Ijaz, I. Ullah, and B. Braaten, "A Compact Dual-Band EMI Metasurface Shield with an Actively Tunable Polarized Lower Band," *IEEE Trans. Electromagn. Compat.*, vol. 54, no. 5, pp. 1182–1185, Oct. 2012.
[30] A. Chatterjee, G. Ali Sarkar, and S. K. Parui, "A Multi-layered Frequency Selective Surface-Based Wireless Filter with Dual Bandpass Response," in *2018 IEEE MTT-S International Microwave and RF Conference (IMaRC)*, Kolkata, India: IEEE, Nov. 2018, pp. 1–4.
[31] G. Xu, S. V. Hum, and G. V. Eleftheriades, "A Technique for Designing Multilayer Multistopband Frequency Selective Surfaces," *IEEE Trans. Antennas Propagat.*, vol. 66, no. 2, pp. 780–789, Feb. 2018.
[32] V. Violi, D. Brizi, and A. Monorchio, "Multi-layer frequency selective surface wideband filter with high selectivity operating in L, S, and C bands," *Sci Rep*, vol. 15, no. 1, p. 26988, Jul. 2025.
[33] P. Wu, F. Bai, Q. Xue, X. Liu, and S. Y. R. Hui, "Use of Frequency-Selective Surface for Suppressing Radio-Frequency Interference from Wireless Charging Pads," *IEEE Trans. Ind. Electron.*, vol. 61, no. 8, pp. 3969–3977, Aug. 2014.
[34] Z. Sun, K. Wang, Y. Mao, J. Hu, W. Zhong, and Y. Yang, "Novel Frequency-Selective Surfaces for Printed Circuit Board-Based Wireless Power Resonators with High Quality Factors," in *2023 IEEE 2nd International Power Electronics and Application Symposium (PEAS)*, Guangzhou, China: IEEE, Nov. 2023, pp. 2436–2440.
[35] Q. Li, F. Arhanifsyah, Z. Sun, R. Liang, J. Yang, and Y. Yang, "A Jerusalem Electromagnetic Compatibility Coat for a Cubic Wireless Charging Container," in *2024 10th International Conference on Power Electronics Systems and Applications (PESA)*, Hong Kong: IEEE, Jun. 2024, pp. 1–5.
[36] A. M. H. Wong, W. Chen, and S. Y. R. Hui, "Magnetic Field Shield Comprising Multiple Frequency Selective Surfaces." US Patent Application No: US 63/896,261, Oct. 09, 2025. (Filed)
[37] W. Chen, B. Xue, K. Li, A. M. H. Wong, and S.-Y. R. Hui, "Multi-Layer Frequency-Selective Surface for Magnetic Field Shielding in Megahertz Wireless Power Transfer Systems," in *2026 IEEE Applied Power Electronics Conference and Exposition (APEC)*, San Antonio, TX, USA, Mar. 2026, pp. 3115-3118.
[38] K. Li, J. Wu, A. C. Yucel, and S.-Y. R. Hui, "New Printed-Circuit-Board Resonators with High Quality Factor and Transmission Efficiency for Mega-Hertz Wireless Power Transfer Applications," *IEEE Trans. Power Electron.*, vol. 38, no. 10, pp. 13207–13218, Oct. 2023.
[39] Qiaowei Yuan, Qiang Chen, Long Li, and K. Sawaya, "Numerical Analysis on Transmission Efficiency of Evanescent Resonant Coupling Wireless Power Transfer System," *IEEE Trans. Antennas Propagat.*, vol. 58, no. 5, pp. 1751–1758, May 2010.